ACS NANO

www.acsnano.org

Article

Electrothermally Induced Channel Formation in a Spin-Crossover Neuron

Elena Salagre,[#] Mahnaz Islam,[#] Yeonju Yu, Sanjana Goyal, Timothy D. Brown, Fatme Jardali, Sangheon Oh, Eric Pop, R. Stanley Williams, A. Alec Talin, Suhas Kumar, Patrick J. Shamberger, and Elliot J. Fuller*

Cite This: *ACS Nano* 2026, 20, 6915−6924

Read Online

ACCESS | Metrics & More | Article Recommendations | Supporting Information

ABSTRACT: There is growing interest in correlated oxides that can switch between volatile resistance states when an electrical bias is applied, functioning as artificial neurons in neuromorphic computing systems. Most devices typically rely on first-order insulator−metal transitions (IMT). However, recent discoveries have shown that devices made of a second-order spin-transition material, such as $LaCoO_3$ (LCO), can exhibit different or improved functionalities. Despite their significance, the microscopic details surrounding the formation of conductive channels have still been unreported. In this study, the spatiotemporal details of channel formation are revealed by using a combination of infrared (IR) and Raman microscopy. Comparison of LCO and materials such as VO_2 reveals critical differences with important ramifications for computing. First, the findings indicate that LCO channels are narrower and more efficient than VO_2, but they are also more sensitive to electric fields and disorder. Channels are found to repeatedly hop between different locations under steady-state oscillations, a behavior not previously reported. Additionally, memory effects at high bias are observed. The experiments, along with finite element simulations (FES), suggest that the spin transition in LCO may significantly influence channel nucleation, leading to an increased sensitivity of neuronal devices to disorder and electrode geometry. We discuss how the inherent stochasticity and memory effects could enable functionalities in neuromorphic computing.

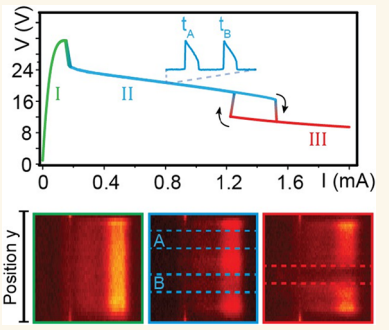

KEYWORDS: *spin crossover, metal−insulator transition, artificial neuron, infrared microscopy, Raman spectroscopy*

INTRODUCTION

Electrically induced insulator−metal transitions (IMT) have been well-documented in materials such as VO_2.[1−5] In switching devices based on such materials, localized fields or Joule heating trigger a phase transition that results in a volatile spike in current or voltage. Under bias, IMT devices can undergo negative differential resistance (NDR) and become locally active, yielding oscillatory or neuron-like spiking dynamics when coupled into networks with passive circuit elements (e.g., resistors and capacitors). Recently, a class of devices based upon a spin crossover induced IMT has been demonstrated using the material LCO, including neuron-like firing, true random number generation, and axon-like signal transmission.[6,7] The spin crossover in LCO is interesting for two reasons: first, it occurs at more technologically relevant temperatures (400−800 K, which is above CMOS operating temperature) unlike materials such as VO_2 (340 K, which is below), and second, it relies on a second-order spin transition and is therefore fundamentally different from previous materials.[8−10] While the macroscopic material properties such as IMT temperature and IMT magnitude are critical to device operation, microscopic details of switching are known to play a considerable role. For example, for VO_2 local inhomogeneities are predicted to form as conductive channels and have been experimentally and theoretically shown to have strong influence on the currents and switching speeds.[11−14] Conduction channels, sometimes termed filaments, are volatile regions smaller than the width of the device that form and concentrate the current flow between the two device electrodes. Revealing the physical mechanisms of channel formation in LCO would provide new opportunities: first, it would enable the development of compact device models for the prediction and rational design of devices, and second, it would reveal the role of the spin transition in channel formation.

Efforts to study conductive channel formation previously have relied upon synchrotron-based dark-field X-ray microscopy, optical reflectance, thermoreflectance, and low-temperature scanning electron microscopy, among others. Previously studied materials include VO_2, V_3O_5, and V_2O_3, which typically

Received: October 16, 2025
Revised: January 27, 2026
Accepted: January 28, 2026
Published: February 13, 2026

https://doi.org/10.1021/acsnano.5c17869
ACS Nano 2026, 20, 6915−6924

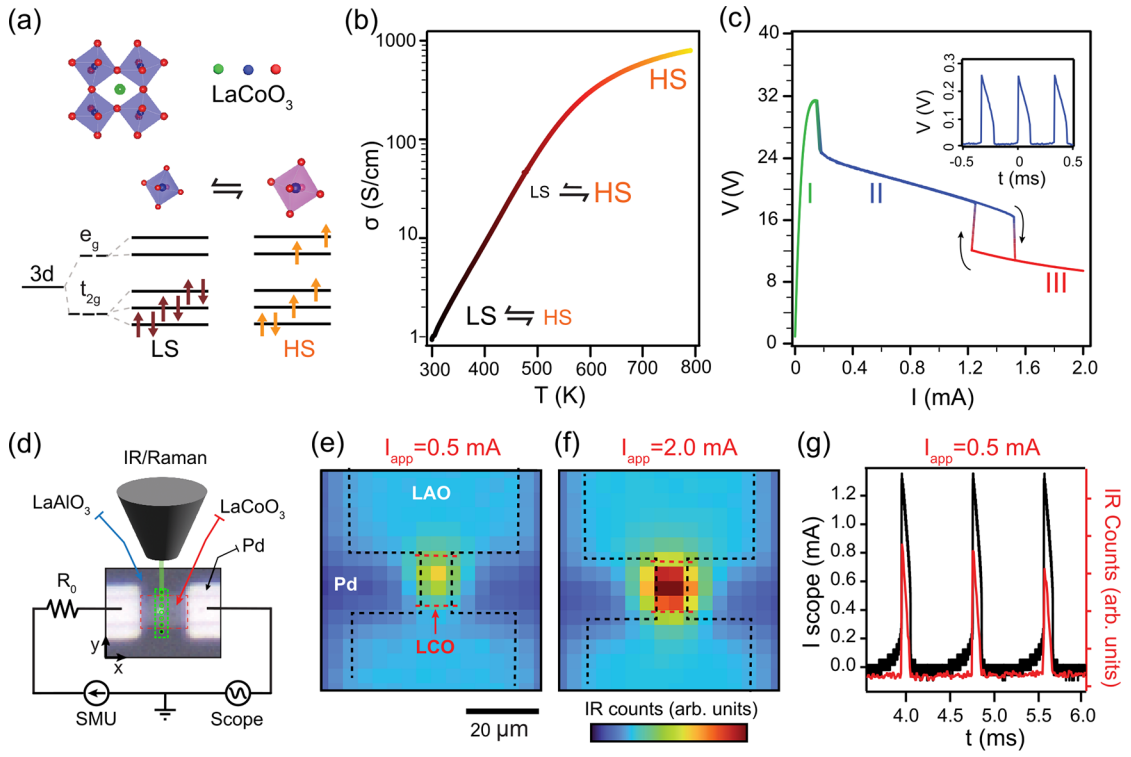

Figure 1. $LaCoO_3$ electrothermal devices with *operando* infrared and Raman imaging: (a) $LaCoO_3$ crystal structure and a simplified spin diagram with a cartoon of Co−O octahedra distortions. (b) Electronic conductivity as a function of temperature. Color scale qualitatively indicates higher ratio of high-spin configuration with temperature from brown to orange. The LS/HS fluctuations are indicated by half arrows with the arrow size indicating qualitatively the ratio between spin states. (c) Current−voltage curve for an L = 8 μm W = 5 μm device with PDR (I), NDR (II), and static NDR (III) regimes indicated in green, blue, and red, respectively. The inset shows 2.9 kHz oscillations at 0.5 mA bias. (d) Schematic of the *operando* experiment including an optical image of an LCO lateral device of L = 8 μm, W = 5 μm, with L along the x axis and W in the y axis. Infrared camera images of L = 6 μm, W = 10 μm LCO device at (e) 0.5 mA bias and (f) 2.0 mA bias. (g) Electrical and thermal oscillations during constant bias regime II of a W = 5 μm device held at I_{app} = 0.5 mA by the SMU.

exhibit channels forming on the order of 5 μm in width or greater.[15−17] For time-resolved pump−probe techniques, repeatable processes are captured while the device is repeatedly switched from zero bias to the NDR regime. Our work has several key differences: first, we consider a spin-transition material in which high-spin and low-spin states coexist in a steady-state mixture as opposed to a first-order transition. Thus, phase coexistence and the spatial distributions of domains and domain boundaries no longer influence the transition. Second, we use high spatial resolution Raman microscopy to determine the conductive channel width and position and combine this with high temporal resolution infrared (IR) imaging to capture real-time switching events under steady-state NDR (without complete cooling and rebiasing). The measurements reveal several critical findings: First, the formation of volatile conductive channels (width <2 μm) is observed during negative differential resistance. Second, during steady-state oscillations, the location of channels are found to be probabilistic, with strong competition observed between narrow, alternating paths. Third, the nucleation of channels is found to be highly sensitive to electric fields due to local disorder but can be engineered by sharp features in contacting electrodes. Finally, we observe channels to progress from volatile, to semivolatile and eventually nonvolatile behavior with increasing current bias (I_{app}), which could be exploited for memory applications.[18,19] Multiphysics finite element simulations (FES) are used to model the local voltages, currents, and electric fields by taking into account the electronic and thermal properties of LCO. FES confirms the observation of current collapsing into a highly conductive channel and the role of electric fields in channel formation.

RESULTS

Electrothermal devices based upon epitaxial LCO (140 nm thick) were grown via pulsed laser deposition on $LaAlO_3$(100) (LAO) single-crystal substrates. The LCO crystal lattice structure and a simplified spin diagram are shown in Figure 1a. In LCO, crystal field splitting lifts the degeneracy of the Co 3d states. The spin pairing energy competes with this effect to promote electrons from low-spin (LS) to higher-spin configurations at higher temperature.[20] While some details remain controversial, it is generally accepted that a first-order transition from a lower spin to higher spin state occurs at 90 K and that a subsequent second-order spin transition occurs from 400 to 800 K and is concomitant with an IMT. This transition is often understood as a spin crossover involving mixtures of low-spin (LS) and high-spin (HS) configurations in different ratios.[21−26] The LCO electronic conductivity as a function of temperature is plotted in Figure 1b. The shape and magnitude of the IMT transition (1−1000 S/cm) is consistent with previous reports of the second-order transition from single crystals and high-quality epitaxial films.[27,28]

All devices exhibited a characteristic current-controlled I−V curve with three distinctive regions, as depicted for a representative device in Figure 1c. The first region (I) is that of positive differential resistance (PDR) where increasing I_{app}

https://doi.org/10.1021/acsnano.5c17869
ACS Nano 2026, 20, 6915−6924

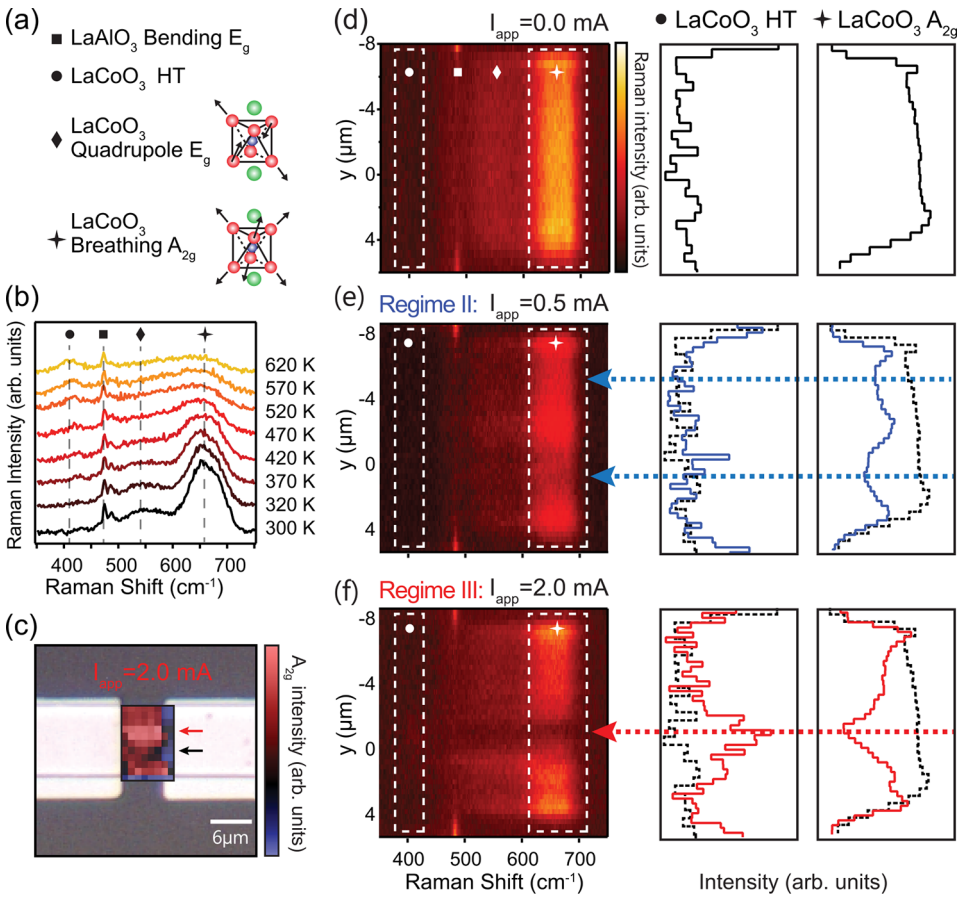

Figure 2. Raman imaging of conductive channels: (a) Schematics of the quadrupole and breathing mode vibrations in LCO indicating atomic motions. (b) Temperature-dependent Raman spectra with temperature indicated at the right. Color of the line indicates an increase in temperature from black to orange. (c) Raman A_{2g} image overlaid across an optical image of a device during 2.0 mA bias. Panels (d–f) correspond to Raman measurements under three bias conditions under 0.0, 0.5, and 2.0 mA bias (three main regions of the $I-V$ curve of a device with $L = 6$ μm, $W = 12$ μm). The left-column Raman images show intensity in color scale; x axis corresponds to Raman shift, and y axis corresponds to the transversal position in the device (perpendicular to current flow). Intensity plots to the right of (d–f) show the distribution of the HT mode and the A_{2g} mode intensity across the device for the three cases.

leads to larger voltages. This first regime is followed by a sudden jump to lower voltage and a second regime (II) characterized by NDR and the emergence of oscillations (see the inset of Figure 1c). It is noted the $I-V$ curve is time averaged by the source-measure unit (SMU), whereas the oscilloscope (inset) captures the relevant oscillations. At higher bias, the oscillations disappear, marking the start of static NDR (III). The exact values at which these regimes occur have a weak dependence on device geometry (SI Section 1, Figure S1).

To reveal the microscopic details of operation, devices were imaged *operando* as depicted in the schematic in Figure 1d. An optical image of a device with dimensions length, $L = 8$ μm, and width, $W = 5$ μm, is shown in the diagram. The LCO devices were connected to a current source, and an oscilloscope was used to capture the oscillations. A limit resistor (5 kΩ) was used to damp the amplitude of oscillations to prevent overheating.[4] Devices were imaged with both an IR camera and a Raman microscope in separate configurations.

First, IR camera movies were recorded during the operation. Figure 1e shows the image of a device taken under 0.5 mA bias, corresponding to regime II and Figure 1f corresponds to 2.0 mA bias and regime III. In both cases, a temperature increase between the Pd contacts is observed, indicating localized heating. Only qualitative trends in temperature rise can be captured due to mixing of infrared emission from the substrate and LCO as well as due to spatial averaging. Data are plotted as raw IR counts (counts increase with temperature). Qualitative spatial and quantitative temporal information can be extracted. For example, a qualitative increase in the temperature is found with increasing applied bias, confirming higher power dissipation. Further, utilizing a high frame-rate camera (Telops M2k), the synchronized thermal and electrical spiking can be measured in real time. As illustrated in Figure 1g, the cyclic behavior observed in regime II is characterized by rises in electrical current accompanied by spikes in the voltage and temperature. The temperature rise is always followed by rapid cooling. Despite the rich temporal information accessible with IR imaging, the resolution was limited to approximately 10 μm and higher-resolution details of operation were captured with Raman microscopy.

Raman spectroscopy with visible light (532 nm) can have a spatial resolution better than 1 μm, and the Raman modes have a well-documented relationship with the spin transition. For example, the quadrupole E_g and breathing mode A_{2g} have been used to track the spin transition as a function of temperature.[29,30] Schematics depicting the atomic motion from quadrupole and breathing mode vibrations are shown in

https://doi.org/10.1021/acsnano.5c17869
ACS Nano 2026, 20, 6915–6924

Figure 2a. At elevated temperature, above 300 K labeled as high temperature (HT), both thermal expansion and the promotion of Co 3d electrons into a higher spin configuration distort the Co−O octahedra and lead to a systematic red shift of the A_{2g} mode. Temperature-dependent Raman spectra of our films are plotted in Figure 2b. At room temperature (black trace), the quadrupole and breathing modes at 550 and 670 cm^{-1} are observed and labeled by diamond and star symbols, respectively. As the temperature increases from 300 to 620 K, the A_{2g} mode undergoes a systematic lowering by ∼15 cm^{-1} and a reduction in overall intensity relative to the baseline. An additional mode near 400 cm^{-1} appears at high temperature as documented previously.[30−32] An example of a Raman micrograph of a device during 2.0 mA biasing (regime III) is plotted in Figure 2c and overlaid across an optical image (on the LCO channel only). Clear inhomogeneities were observed as modulation in A_{2g} and a linear feature with lower intensity is observed connecting the two electrodes (indicated by the black arrow). A lower bound on the temperature in the hottest region (approximately 600 K) can be approximated by comparison with the temperature-dependent Raman measurements, as shown in the SI Section 2, Figure S2. The shape and size of the conduction channel was confirmed by biasing to the damage threshold (>3.0 mA) in which case a permanent optical contrast over the same region is observed (see SI Section 3, Figure S3). We found close agreement between Raman and IR imaging in the positions of conduction channels.

Having established conduction channels as linear features across Raman images, we took Raman line cuts at points across the center of the LCO channel, as indicated by the dotted green line in Figure 1d. These line cuts allow detailed comparisons between hot and cold regions while reducing redundancy in the data sets. In the 2D plot shown in Figure 2d−f, Raman intensity (color scale) is plotted against the wavenumber (x axis) and vertical position within the LCO channel (y axis). These plots are shown for a device under 0.0, 0.5, and 2.0 mA bias corresponding to the regimes I, II and III, respectively. In regime I, a vertical bright yellow line between 600 and 700 cm^{-1} corresponds to the breathing mode of LCO (indicated by white star) and is roughly uniform across the device width (y axis). The edges of the LCO channel are marked by a loss of signal at 670 cm^{-1} and a feature at 490 cm^{-1} from the underlying substrate (white square).[33] The intensity distributions for the high temperature (400 cm^{-1}) and breathing modes (670 cm^{-1}) are shown to the right of each image, with arrows indicating most affected positions.

We next discuss regime III depicted in Figure 2f, as its interpretation is more straightforward than regime II. A channel is observed as a central black horizontal line (broader A_{2g} with lower counts) in the Raman image, indicated with a red arrow. The associated increase in the high temperature mode at 400 cm^{-1} is clear from the intensity distributions. The Raman features are similar to the channel in Figure 2c and similar to Figure 2b curves at a high temperature. A temperature estimate based upon peak position gives a lower bound of 600 K for the conduction channel temperature. Additionally, the sides of this high temperature channel exhibit an increase in the A_{2g} intensity and wavenumber. This indicates effects outside of pure temperature and may be related to strain. Features observed in regime III conduction channels were dependent on total dissipated power across the device, as is the case for other materials (SI Figure S4) and consistent across many devices (SI Figure S5 bottom row).

Regime II presents significantly more complex behavior with intriguing ramifications for LCO device physics, especially considering that dynamic oscillations occur. In the example in Figure 2e, two channels are observed (indicated by blue arrows) with a decrease in the A_{2g} mode intensity less pronounced than in regime III. The middle and right columns of Figure 2d−f correspond to the intensity distribution of the A_{2g} and the high temperature 400 cm^{-1} mode, respectively. In Figure 2e, the two features are found to be of a similar nature to those in regime III (seen in Figure 2f). A comparison between regimes II and III reveals that despite the similar overall width of the conduction channels, regime II shows a less pronounced decrease in intensity in those regions. Interestingly, only regime III is shown to have significant increase in the mode at 400 cm^{-1}, probably due to time averaging across this low intensity feature in regime II. Further interpretation of regime II is complicated by the time-averaged nature of the Raman mapping (∼4 h duration). For example, the peak temperature of oscillations will be significantly higher than the measured average, and therefore, we cannot attempt to compare peak channel temperature directly between regimes II and III. Further examples of Raman imaging at bias levels in regimes II and III are found in SI Figure S6.

Because individual oscillations cannot be captured in Raman spectroscopy due to their short timescale (<1 ms, see SI Figure S7), an intriguing question arises as to whether spatially separate conduction channels can occur simultaneously or whether they nucleate separately and probabilistically over the total period of measurement during oscillating NDR. In the latter case, the Raman profile in Figure 2e would then reflect the probability distribution of competing current pathways at the surface. When looking at multiple devices, we find that regime II is highly sensitive to inhomogeneities and disorder with significant sample-to-sample variability observed (see Figure S5 top row). This is in contrast to regime III which was consistent across multiple devices, showing a single current path. Regime II distributions can be grouped into three categories: (1) many conduction channels (temperature decreases relatively uniformly across the channel); (2) two or three favorable spots dominating (e.g. Figure 2e); and (3) single conduction path dominating, where only one region is affected. Nonetheless, all observations during regime II occur with oscillations. We conclude that for regime II, multiple competing conduction paths potentially create a distribution that is highly sensitive to local disorder. In contrast, for regime III, the formed path is static and takes a definitive position. For further interpretation of regime II, we extend our observations into the time domain.

We aimed to address whether conduction channels are due to simultaneous uneven current flow or due to probabilistic paths forming during each oscillation in NDR. Assuming conduction channel formation arises from a probabilistic process driven by spin fluctuations that are sensitive to local electric fields, we hypothesized that fields from device electrodes could be used to tilt the probability systematically. This would simplify the interpretation relative to the disordered case. To test this, we created an additional device geometry with two hot spots in the electric field (bistable device) compared to our uniform devices already presented. The simulated electric field from uniform and bistable device geometries are depicted in Figure 3a and Figure 3b,

https://doi.org/10.1021/acsnano.5c17869
ACS Nano 2026, 20, 6915−6924

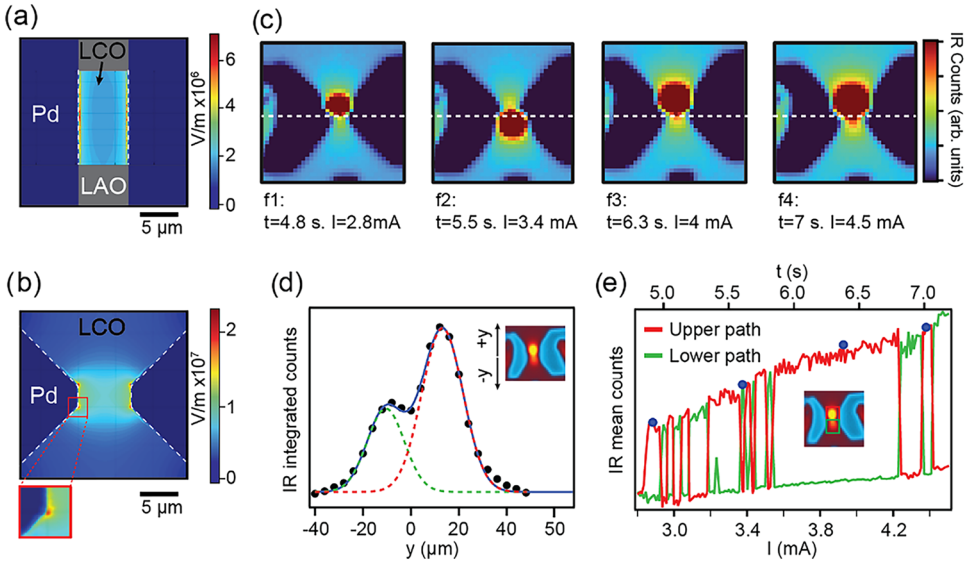

Figure 3. Role of electric field on probability distribution of conduction channel formation: (a, b) Results for electric field models for uniform and bistable devices at $t = 0$ upon a 2 mA applied bias. An inset showing the electrode corner in panel (b) is shown below, corresponding to the region inside the red square. (c) Experimental thermal camera measurements of a device in oscillatory regime showing the bistable position of the conduction channel. (d) Time-averaged intensity counts in the LCO channel showing the bistable distribution of conductive paths. (e) Mean counts in the upper (red) and lower (green) parts of the device as a function of I_{app} and time. Insets in panels (d, e) show integration regions. Blue circles in panel (e) correspond to the frames shown in panel (c).

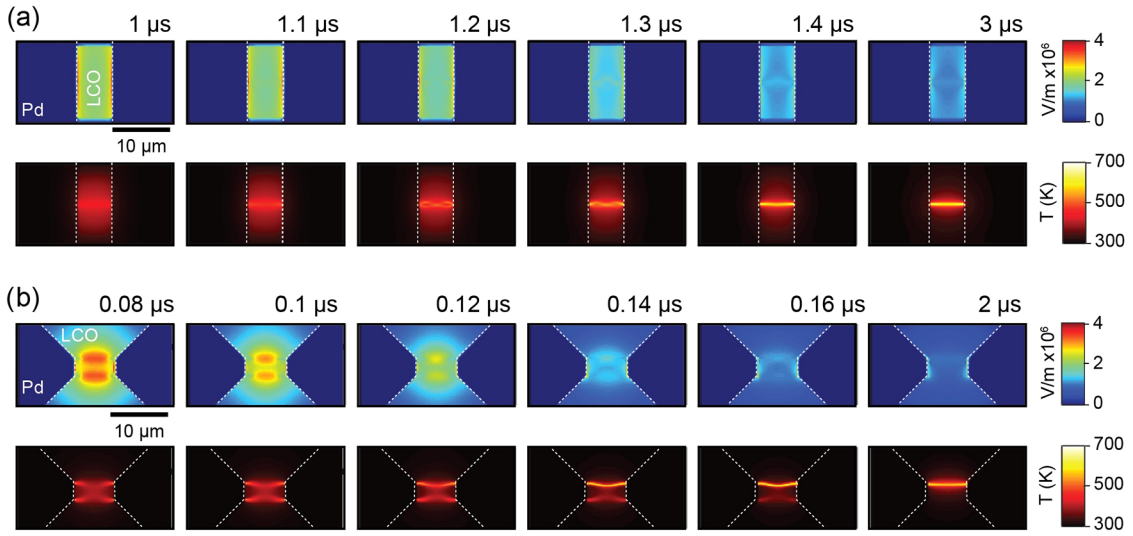

Figure 4. Time evolution of the finite element model for field and temperature distributions in (a) uniform and (b) bistable devices. Color scales for field (V/m) and temperature (K) are shown on the right of each row. Electrodes are indicated by dashed white lines. Time stamps are shown at the top of the field images for each column and are different for each device geometry. The last column, 3 and 2 μs, denotes the steady state. Simulations consider a device with a 2.0 mA bias.

respectively. In contrast with Figure 3a, Figure 3b has two lobes near sharp electrode edges (see the inset). Our hypothesis was that a bistable device will generate a bimodal probability distribution in the current pathway formation (as opposed to random due to disorder), which can be clearly resolved spatially and temporally through IR imaging.

Figure 3c corresponds to the frames extracted from an IR thermal video of a bistable device ($L = W = 5$ μm). The device was ramped within the current bias range spanning regime II, where oscillations occur. Full details about time, applied current, and voltage curves can be found in SI Section 7, Figure S10. Four representative spiking events (f1, f2, f3, f4) show a hot spot of increasing temperature with current. We observe a bistable distribution, where current collapse (hot spot seen as red area) can either happen above or below the center of the channel (indicated by a dashed white line), near the regions of high field. If the intensity is integrated for the whole oscillatory regime, this bistable nature is made evident, as shown in Figure 3d and fitted to the upper and lower Gaussian distributions (red and green). We note that the probability is affected by increasing bias and temperature as well as field asymmetry.

The IR count distribution is further complicated by localized IR screening due to the metal electrodes (SI Figure S11 and Discussion). Nevertheless, Figure 3e depicts the mean intensity of upper and lower area boxes (shown in the inset), which highlights the nonsimultaneous nature of the competing

https://doi.org/10.1021/acsnano.5c17869
ACS Nano 2026, 20, 6915−6924

current paths. The center of the hot region, in red, moves from top to bottom of the device channel, never appearing in both simultaneously. While individual oscillations are not easily extracted due to limited frame rate with our 10 μm resolution camera, the change in the hot channel position is clear. Together with the temporal resolution of individual nucleation events, this strongly suggests competing nonsimultaneous filaments. Similar experiments, both maintaining constant bias in the oscillatory regime and cycling a device to the static regime III multiple times, have been performed, which also indicate a bimodal distribution between high-field regions in bistable devices (SI Figure S12).

Simulations were carried out to capture the time-dependent formation of hot conductive channels. The 3D model couples electronic transport and heat transfer in solids using the COMSOL Multiphysics commercial software package, which governs Joule heating law (more details in the Methods section and SI Section 9).[34] Critically, the simulations take into account the temperature-dependent electrical conductivity from Figure 1b by interpolating the curve during the time steps. The two types of electrode geometries from Figure 3a,b were simulated. Time series showing electric field and temperature evolution for uniform and bistable field devices are shown in Figure 4a,b, respectively. Simulations shown consider a 2.0 mA applied bias, consistent with our experimental results. In the uniform field simulations in Figure 4a, the central region begins to concentrate most of the temperature and current. The temperature gradient gets sharper with time and eventually collapses current and heat into a conduction channel, bridging the electrodes. For the bistable case, Figure 4b, the field presents two regions of higher intensity on the top and bottom of the channel. Electrode geometry creates localized charge accumulation at the sharp electrode edges, which leads to a high current density. The temperature gradually shifts from asymmetric bistability to a single dominant path. The timescales observed for the collapse event are found to depend strongly on material properties and local electric field strength but are usually on the 0.1−1.0 μs timescale. To investigate the effect of geometry and substrate, as well as discern intrinsic material implications, we have performed a sensitivity analysis that can be seen in SI Section 9. Finally, additional modeling including the effects of elastic strain indicate large gradients (as much as 1%) occurring at the edges of the conduction channel. Large strain gradients may explain the shifts observed at the edges of the conduction channel, but such effects require further experiments to verify (see SI Figures S13 and S14 for further discussion).

To complete our description of the device behavior, we discuss observations of semivolatile and nonvolatile conduction channels. In the preceding discussion, volatility is observed when current does not exceed the start of regime III (~2.0 mA) for extended periods. Longer-term residual effects are found at higher bias ($2.0 < I < 3.0$ mA) for the device geometries presented here. This effect, seen in Figure 5a, consists of a ~5 cm^{-1} red shift and intensity decrease of the A_{2g} mode in the center of what constituted the active conduction channel. Additional changes in boundary regions can also be observed, usually involving a blue shift in those areas. It also induces a change in the NDR regimes to lower voltages and lower current bias thresholds (Figure 5b and SI Figure S12b). The signatures last a few hours, with the specific timescales varying due to the duration of current hold and voltage. We note that for VO_2 devices, a similar observation has been

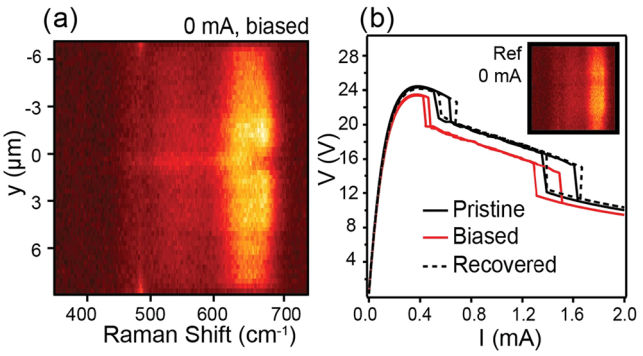

Figure 5. Nonvolatile memory effects in channel formation correlated with $I-V$ characteristics. (a) Raman image taken at 0.0 mA bias for a device ($W = 15$ μm, $L = 7$ μm) that was previously held at 2.0 mA for 3 h. Panel (b) shows corresponding $I-V$ curve before the hold (black), after the hold (red), and after relaxation over several days (dashed black). The inset Raman image in (b) corresponds to the same device before bias holds for reference.

ascribed to either point defects or pinning of domains.[18] Later, we discuss the possible mechanisms for such nonvolatility.

DISCUSSION

Having established the nature of conduction channel formation in LCO devices, we next discuss how our observations compare with those of other materials and their implications for device physics. First, our results are consistent with previous theoretical and experimental work. In 1963, Ridley predicted NDR and conductive channel formation in materials under current biasing due to channels possessing a more stable thermodynamical state via entropy production minimization.[35] More recently, Bradicich et al. were able to model conduction channel formation in VO_2 using FES without the energetics of phase boundaries, although they utilized the much sharper IMT transition.[34] In another example, Jardali et al. demonstrated through analytical models that the NDR regime can be accessed without the sharp non-nonlinearities from first-order materials, although they did not explicitly model channel formation.[36] The results are also consistent with the experimental observation of channels in second-order V_3O_5.

We found that LCO produced narrower channels at ~2 μm compared to studies of vanadium oxides with ~5 to 10 μm channels. Channel nucleation and width has been linked to resistivity ratios in the material's IMT for vanadium oxides,[37,38] with larger ratio materials expected to produce narrower channels. This relationship does not appear to extend directly to LCO, as it would predict larger channels not smaller. We found that when considering differences between LCO and vanadium oxide studies, both extrinsic differences (i.e., device dimensions, substrate) and competing intrinsic differences (IMT transition, thermal conductivity) must be considered. However, FES analysis indicated that extrinsic factors are unlikely to explain smaller LCO channels. For example, a sensitivity analysis revealed substrate thermal conductivity and device dimensions could not explain the smaller channels alone (SI Section 9.1.2). We therefore conclude that intrinsic materials properties are likely responsible. From the literature, we found that broadly, channel width has a strong correlation with total power dissipated, as seen across multiple studies independent of many other factors. The total power is significantly lower for LCO than reported channels in materials such as VO_2 (refer to SI Figure S4d,e).[39−44] The required

https://doi.org/10.1021/acsnano.5c17869
ACS Nano 2026, 20, 6915−6924

power for NDR can be linked to several competing intrinsic material properties, such as thermal conductivity and IMT resistance ratio, but it is difficult to completely disentangle these effects from modeling. While IMT ratio and LCO thermal conductivity both appeared to play a role in FES, further work outside the scope of this study would be required to fully quantify the relationships. We also note that the lower power for LCO devices and the more gradual nature of the transition should increase oscillation endurance and lower energy consumption.

Conduction channels in LCO devices exhibit a probabilistic nature. In contrast to the formation of static pathways, these channels tend to hop between locations. This phenomenon of hopping is found to occur between consecutive oscillations and between successive static NDR cycles. We note that such observations were found among nearly all LCO devices with more than one sharp electrode point. Previously, Del Valle et al. looked at cycle-to-cycle conduction channel formation during the nucleation event and just after current path percolation. The study was done in both first-order materials V_2O_3 and VO_2 and the second-order material V_3O_5, where the devices were allowed to completely cool between cycles.[37] More recently, probabilistic, competing conduction paths were observed in materials cycle-to-cycle, but devices were not investigated or discussed under steady-state oscillation, as we have shown in this work.[45,46] Adda et al. report channel formation during cycling and steady state bias on V_3O_5 as we have discussed for LCO.[16] However, they conclude the presence of a wide single conduction channel during oscillations rather than probabilistic hopping. The material and substrate thermal properties, as well as the magnitude of thermal fluctuations, are crucial to the emergence of hopping. For example, the residual temperature from a previous filament can influence the following nucleation event if temperature is not sufficiently distributed or dissipated. As an example, we observed that competition between filaments tended to decrease with applied bias and the baseline temperature rise (Figure 3e). This indicates that residual temperature likely influences nucleation but is not enough to overcome competition between bistable regions. Additionally, we note that it remains unclear whether hopping of narrow conduction paths during oscillations is limited to LCO or extends to other materials. Future work utilizing the techniques presented here would help determine universality during oscillation (e.g., comparing LCO with V_3O_5).

It is interesting to discuss the potential processes governing probabilistic formation, as they may explain the observed differences with other materials. We hypothesize that the spin gap, which is roughly 30 meV and sits near the thermal energy at 300 K (~25 meV), may act as a source of the observed hopping in conduction channel formation when coupled to thermal fluctuations. The prevailing picture of the spin crossover involves constant fluctuation between spin states in an equilibrium (as depicted in Figure 1a), but where each spin promotion event could lead to significant structural distortions and large highly localized changes in conductivity. The large conductance fluctuations accessible at room temperature may effectively sample a large potential energy landscape due to electric fields and disorder, giving rise to competition between more regions when compared with other materials. For example, conductance fluctuations in second-order V_3O_5 may be sufficiently small (due the shallow transition) as to only sample a small space that governs nucleation. Similarly, for VO_2, thermally excited conductance fluctuations are not enough to overcome the transition, and thus nucleation may be dominated by weak conductance fluctuations in the insulating state with nucleation properties similar to those of V_3O_5. The spin gap associated with spin fluctuations depends on the octahedral field splitting and therefore could be engineered through alloying LCO (e.g., Sm alloying) or other transition metal oxides.[47,48]

Another interesting similarity with VO_2 is the observation of memory effects, including semivolatile and nonvolatile behaviors. Such memory effects are well-documented in VO_2 with hysteresis in domain formation from both electrothermal switching and temperature cycling.[15,18,19,49] For VO_2, the origin of short-term memory remains unresolved but has been hypothesized to relate to the energetics of domain flipping and potentially due to the migration or movement of point defects.[18,38] For LCO, the temperatures (600−800 K) and timescales (hours to days) suggest that oxygen vacancy diffusion may play a role. Thermodynamically, we expect a nonzero population of vacancies created during growth. These defects may redistribute under bias, driven by the local temperature, strain, and voltage gradients surrounding the conductive channel. A thorough investigation of these phenomena is beyond the scope of this work. However, the findings presented herein will serve as motivation for the local characterization of chemical and structural changes. While these effects inhibit repeatable behavior at high bias, they may prove useful for neuromorphic algorithms which utilize short-term plasticity in neuronal firing for training.[44,50−52] We note that these effects could be responsible for VO_2 memory as well, indicating that the energetics for domain flipping may be only partially responsible.

CONCLUSION

For LCO, the details of switching and channel formation appear to have qualitatively different behavior compared to other oxides. In particular, the size of channels appears to be significantly smaller than VO_2 for similar geometries, despite the gradual nature of the LCO transition. This is counter to previous trends with vanadium oxides, where shallower transitions are found to support larger conduction channels. A sensitivity to local electric fields from disorder or contacting electrodes is found to give rise to repeated stochastic hopping or strong competition between conduction paths under steady-state oscillations. Although the precise details surrounding the hopping nucleation events are unknown, the low energy of the spin gap presents an intriguing hypothesis. Further opportunities lie in the study of other spin-transition materials (i.e., organic spin complexes) and the engineering oxide spin crossover devices. For example, rare-earth substitutions (e.g., with other lanthanides[28] or strontium) are a well-known method to increase the crystal field splitting or to tune the octahedral tilt which will have a direct impact on the transition through modifications to spin states and thermal conductivity.

METHODS

Growth and Device Fabrication

For pulsed laser deposition, the $LaCoO_3$ target was purchased from Toshima corporation and ablated with 3 J/cm^2 power using an Nd:YAG laser with a wavelength of 266 nm. After verifying electrical and structural properties, devices were fabricated using a two-step lithography process involving first etching of the channels to specific dimensions and then depositing metal contacts. First, channels were

https://doi.org/10.1021/acsnano.5c17869
ACS Nano 2026, 20, 6915−6924

etched with an MRC Model 55 reactive ion etching system and Freon 23 gas with 100 W of power and a partial pressure of 10 mTorr. A following lithography step is used to define and construct the electrode geometries and contact pads using 150 nm of Pd deposited by electron beam evaporation. Channel dimensions varied from roughly 2−15 μm in width (W) and 2−10 μm in length (L).

Device Characterization

A limiting resistance of 5.1 kΩ was used to avoid damaging the device during biasing. Current sweeps were performed with a Agilent B2901A precision source/measure unit, and a Agilent Technologies MSO7054A oscilloscope was used to record oscillations. The devices were wire bonded to a gold chip holder that is attached with thermal paste to a metal block to improve mechanical and thermal anchoring. The devices were operated at room temperature and in an atmosphere to prevent the formation of oxygen vacancy defects. The overall chip temperature was measured with the thermal camera and checked that it was at room temperature (around 295 K) during all regimes of operation. The IV curves and voltage values given in this paper are across the device, and the contribution from the load resistor has been removed.

Infrared Imaging

IR imaging of the LCO devices was performed using an FLIR SC-6700 and a Telops M2k UD. Movies taken with the FLIR SC-6700 infrared camera were analyzed using FLIR Research Studio software. The camera's sampling rate was set at 62.9, 1369.1, and 2055.2 Hz for different measurements, and the temperature scale used were 35−150 and 80−200 C. Pixel size is 4 μm and the observed spatial resolution of approximately 10 μm (detector pitch 15 μm frame size 160 × 128 pixels). The temporally resolved measurements of the oscillations were performed using a Telops M2k UD (detector pitch 30 μm, frame size 64 × 4 pixels), 5.61 μs exposure time, and 90 kHz frame rate. Absolute temperature values cannot be extracted due to the substrate and environment IR contributions, which cannot be decoupled. Therefore, only IR counts are used as an indicator of temperature.

Raman Spectroscopy

Raman spectroscopy was performed on a Renishaw inVia commercial Raman microscope with resolution <1 μm. For line scans and two-dimensional images, a step of 0.1−0.5 μm was used to obtain a balance between measurement time and resolution. Each point is integrated for ∼5 to 10 min, with total time for each measurement ranging from 1 to 6 h depending on the device size. For *operando* measurements, the device is held at a constant bias during acquisition time, with its voltage and oscillations (when applicable) being monitored. The measurements are performed with a 532 nm laser and ∼220 μW to avoid external heating of the sample.

Finite Element Simulations

Finite element modeling was carried out using COMSOL Multiphysics, with electrical and thermal models coupled via the Joule heating module. The model consists of palladium (Pd) electrodes at the top, followed by a layer of lanthanum cobaltite (LCO), and a lanthanum aluminate (LAO) substrate beneath (see more details in SI Section 9). To investigate the electrothermal response of the device, temperature-dependent material properties, including electrical conductivity, thermal conductivity, and heat capacity, were imported into the simulation based on measured and previously reported data, see SI Section 9, Table S1.

■ ASSOCIATED CONTENT

Supporting Information

The Supporting Information is available free of charge at https://pubs.acs.org/doi/10.1021/acsnano.5c17869.

Supporting $I-V$ curves for LCO devices of different sizes; additional optical, thermal, and Raman maps; additional analysis and bibliographic survey of conductive channel widths; analysis of Raman spectra at different temperatures; details about analysis of nonuniform devices and bistability; and details and additional results for the finite element simulations and sensitivity analysis (PDF)

■ AUTHOR INFORMATION

Corresponding Author

Elliot J. Fuller − *Sandia National Laboratories, Livermore, California 94550, United States;* orcid.org/0000-0001-7912-8688; Email: ejfull@sandia.gov

Authors

Elena Salagre − *Sandia National Laboratories, Livermore, California 94550, United States;* orcid.org/0000-0001-9672-9987

Mahnaz Islam − *Sandia National Laboratories, Livermore, California 94550, United States; Department of Electrical Engineering, Stanford University, Stanford, California 94305, United States*

Yeonju Yu − *Department of Materials Science and Engineering, Texas A&M University, College Station, Texas 77843-3003, United States*

Sanjana Goyal − *Sandia National Laboratories, Livermore, California 94550, United States; Department of Engineering Science, UC Berkeley, Berkeley, California 94720, United States;* orcid.org/0009-0000-0108-8188

Timothy D. Brown − *Sandia National Laboratories, Livermore, California 94550, United States*

Fatme Jardali − *Department of Materials Science and Engineering, Texas A&M University, College Station, Texas 77843-3003, United States*

Sangheon Oh − *Sandia National Laboratories, Livermore, California 94550, United States;* orcid.org/0000-0003-2371-7410

Eric Pop − *Department of Electrical Engineering, Stanford University, Stanford, California 94305, United States;* orcid.org/0000-0003-0436-8534

R. Stanley Williams − *Department of Electrical and Computer Engineering, Texas A&M University, College Station, Texas 77843-3128, United States;* orcid.org/0000-0003-0213-4259

A. Alec Talin − *Sandia National Laboratories, Livermore, California 94550, United States;* orcid.org/0000-0002-1102-680X

Suhas Kumar − *Sandia National Laboratories, Livermore, California 94550, United States;* orcid.org/0000-0002-6772-7250

Patrick J. Shamberger − *Department of Materials Science and Engineering, Texas A&M University, College Station, Texas 77843-3003, United States;* orcid.org/0000-0002-8737-6064

Complete contact information is available at: https://pubs.acs.org/10.1021/acsnano.5c17869

Author Contributions

#E.S. and M.I. contributed equally to this work.

Notes

The authors declare no competing financial interest.

https://doi.org/10.1021/acsnano.5c17869
ACS Nano 2026, 20, 6915−6924

■ ACKNOWLEDGMENTS

This work was supported as part of the Center for Reconfigurable Electronic Materials Inspired by Nonlinear Neuron Dynamics (ReMIND), an Energy Frontier Research Center funded by the US Department of Energy (DOE), Office of Science, Basic Energy Sciences. This paper describes objective technical results and analyses. Any subjective views or opinions that might be expressed in the paper do not necessarily represent the views of the US DOE or the United States Government. M.I. and S.O. were additionally supported by the Sandia Laboratory-Directed Research and Development (LDRD) Program. Sandia National Laboratories is a multimission laboratory managed and operated by National Technology and Engineering Solutions of Sandia, LLC., a wholly owned subsidiary of Honeywell International, Inc., for the US Department of Energy's National Nuclear Security Administration under contract DE-NA-0003525. The views expressed in the article do not necessarily represent the views of the US Department of Energy or the United States Government.

■ REFERENCES

(1) Duchene, J.; Terraillon, M.; Pailly, P.; Adam, G. Filamentary Conduction in VO_2 Coplanar Thin-Film Devices. *Appl. Phys. Lett.* **1971**, *19*, 115−117.
(2) Yang, Z.; Ko, C.; Ramanathan, S. Oxide Electronics Utilizing Ultrafast Metal-Insulator Transitions. *Annu. Rev. Mater. Res.* **2011**, *41*, 337−367.
(3) Zimmers, A.; Aigouy, L.; Mortier, M.; Sharoni, A.; Wang, S.; West, K. G.; Ramirez, J. G.; Schuller, I. K. Role of Thermal Heating on the Voltage Induced Insulator-Metal Transition in *VO_2*. *Phys. Rev. Lett.* **2013**, *110*, No. 056601.
(4) Brown, T. D.; Bohaichuk, S. M.; Islam, M.; Kumar, S.; Pop, E.; Williams, R. S. Electro-Thermal Characterization of Dynamical VO_2 Memristors via Local Activity Modeling. *Adv. Mater.* **2023**, *35*, No. 2205451.
(5) Schofield, P.; Bradicich, A.; Gurrola, R. M.; Zhang, Y.; Brown, T. D.; Pharr, M.; Shamberger, P. J.; Banerjee, S. Harnessing the Metal−Insulator Transition of VO_2 in Neuromorphic Computing. *Adv. Mater.* **2023**, *35*, No. 2205294.
(6) Brown, T. D.; Zhang, A.; Nitta, F. U.; Grant, E. D.; Chong, J. L.; Zhu, J.; Radhakr-Ishnan, S.; Islam, M.; Fuller, E. J.; Talin, A. A.; Shamberger, P. J.; Pop, E.; Williams, R. S.; Kumar, S. Axon-like active signal transmission. *Nature* **2024**, *633*, 804−810.
(7) Woo, K. S.; Zhang, A.; Arabelo, A.; Brown, T. D.; Park, M.; Talin, A. A.; Fuller, E. J.; Bisht, R. S.; Qian, X.; Arroyave, R.; Ramanathan, S.; Thomas, L.; Williams, R. S.; Kumar, S. True random number generation using the spin crossover in $LaCoO_3$. *Nat. Commun.* **2024**, *15*, No. 4656.
(8) Rata, A. D.; Herklotz, A.; Schultz, L.; Dörr, K. Lattice structure and magnetization of $LaCoO_3$ thin films. *Eur. Phys. J. B* **2010**, *76*, 215−219.
(9) Rotter, M.; Wang, Z.-S.; Boothroyd, A. T.; Prabhakaran, D.; Tanaka, A.; Doerr, M. Mechanism of spin crossover in $LaCoO_3$ resolved by shape magnetostriction in pulsed magnetic fields. *Sci. Rep.* **2014**, *4*, No. 7003.
(10) Zhou, G.; Wang, X.; Ji, H.; Zhang, J.; Kang, P.; Li, Z.; Xu, X. The strain induced magnetic and anisotropic variations of $LaCoO_3$ thin films. *J. Magn. Magn. Mater.* **2020**, *515*, No. 167303.
(11) Woo, K. S.; Williams, R. S.; Kumar, S. Localized Conduction Channels in Memristors. *Chem. Rev.* **2025**, *125*, 294−325.
(12) Kumar, S.; Williams, R. S. Separation of current density and electric field domains caused by nonlinear electronic instabilities. *Nat. Commun.* **2018**, *9*, No. 2030.
(13) Islam, M.; Bohaichuk, S.; Brown, T.; Oh, S.; Perez, C.; Zhang, C.; Park, T.; Park, M.; Talin, A.; Ramanathan, S.; Kumar, S.; Pop, E. An Electro-Optical Mott Neuron Based on Niobium Dioxide. *Nat. Electron.* **2025**, *8*, 672−679.
(14) Islam, M.; Bohaichuk, S. M.; Brown, T. D.; Oh, S.; Perez, C.; Zhang, C.; Park, T. J.; Park, M.; Talin, A. A.; Ramanathan, S.; Kumar, S.; Pop, E. An electro-optical Mott neuron based on niobium dioxide. *Nat. Electron.* **2025**, *8*, 672−679.
(15) Kisiel, E.; Salev, P.; Poudyal, I.; Alspaugh, D. J.; Carneiro, F.; Qiu, E.; Rodolakis, F.; Zhang, Z.; Shpyrko, O. G.; Rozenberg, M.; Schuller, I. K.; Islam, Z.; Frano, A. High-Resolution Full-Field Structural Microscopy of the Voltage-Induced Filament Formation in VO_2-Based Neuromorphic Devices. *ACS Nano* **2025**, *19*, 15385−15394.
(16) Adda, C.; Lee, M.-H.; Kalcheim, Y.; Salev, P.; Rocco, R.; Vargas, N. M.; Ghazikhanian, N.; Li, C.-P.; Albright, G.; Rozenberg, M.; Schuller, I. K. Direct Observation of the Electrically Triggered Insulator-Metal Transition in V_3O_5 Far below the Transition Temperature. *Phys. Rev. X* **2022**, *12*, No. 011025.
(17) Guénon, S.; Scharinger, S.; Wang, S.; Ramírez, J. G.; Koelle, D.; Kleiner, R.; Schuller, I. K. Electrical breakdown in a V_2O_3 device at the insulator-to-metal transition. *Europhys. Lett.* **2013**, *101*, No. 57003.
(18) Basak, S.; Sun, Y.; Banguero, M. A.; Salev, P.; Schuller, I. K.; Aigouy, L.; Carlson, E. W.; Zimmers, A. Spatially Distributed Ramp Reversal Memory in VO_2. *Adv. Electron. Mater.* **2023**, *9*, No. 2300085.
(19) Rana, A.; Li, C.; Koster, G.; Hilgenkamp, H. Resistive switching studies in VO_2 thin films. *Sci. Rep.* **2020**, *10*, No. 3293.
(20) Jia, T.; Hao, Y.; Hao, H. The spin-state effect on the redox performance of $LaCoO_3$ perovskites. *Results Phys.* **2024**, *61*, No. 107766.
(21) Ishimoto, T.; Ito, Y.; Tada, T.; Oike, R.; Nakamura, T.; Amezawa, K.; Koyama, M. Theoretical study on temperature effect of electronic structure and spin state in $LaCoO_3$ by using density functional theory. *Solid State Ionics* **2016**, *285*, 195−201.
(22) Abbate, M.; Fuggle, J. C.; Fujimori, A.; Tjeng, L. H.; Chen, C. T.; Potze, R.; Sawatzky, G. A.; Eisaki, H.; Uchida, S. Electronic structure and spin-state transition of *$LaCoO_3$*. *Phys. Rev. B* **1993**, *47*, No. 16124.
(23) Ikeda, A.; Matsuda, Y. H.; Sato, K.; Nasu, J. A Review on Magnetic Field Induced Spin Crossover in $LaCoO_3$ up to 600 T. *J. Phys. Soc. Jpn.* **2024**, *93*, No. 121005, DOI: 10.7566/jpsj.93.121005.
(24) Takegami, D.; Tanaka, A.; Agrestini, S.; Hu, Z.; Weinen, J.; Rotter, M.; Schüßler-Langeheine, C.; Willers, T.; Koethe, T. C.; Lorenz, T.; Liao, Y. F.; Tsuei, K. D.; Lin, H.-J.; Chen, C. T.; Tjeng, L. H. Paramagnetic LaCoO3: A Highly Inhomogeneous Mixed Spin-State System. *Phys. Rev. X* **2023**, *13*, No. 011037.
(25) Haverkort, M. W.; Hu, Z.; Cezar, J. C.; Burnus, T.; Hartmann, H.; Reuther, M.; Zobel, C.; Lorenz, T.; Tanaka, A.; Brookes, N. B.; Hsieh, H. H.; Lin, H.-J.; Chen, C. T.; Tjeng, L. H. Spin state transition in $LaCoO_3$ studied using soft x-ray absorption spectroscopy and magnetic circular dichroism. *Phys. Rev. Lett.* **2006**, *97*, No. 176405.
(26) Haverkort, M. W.; Hu, Z.; Cezar, J. C.; Burnus, T.; Hartmann, H.; Reuther, M.; Zobel, C.; Lorenz, T.; Tanaka, A.; Brookes, N. B.; Hsieh, H. H.; Lin, H.-J.; Chen, C. T.; Tjeng, L. H. Spin State Transition in $LaCoO_3$ Studied Using Soft X-ray Absorption Spectroscopy and Magnetic Circular Dichroism. *Phys. Rev. Lett.* **2006**, *97*, No. 176405.
(27) Yamaguchi, S.; Okimoto, Y.; Tokura, Y. Bandwidth dependence of insulator-metal transitions in perovskite cobalt oxides. *Phys. Rev. B* **1996**, *54*, No. R11022.
(28) Zhang, A.; Oh, S.; Choi, B. K.; Rotenberg, E.; Brown, T. D.; Spataru, C. D.; Kinig-Stein, E.; Guo, J.; Sugar, J. D.; Salagre, E.; Mascaraque, A.; Michel, E. G.; Shad, A. C.; Zhu, J.; Witman, M. D.; Kumar, S.; Talin, A. A.; Fuller, E. J. Tuning the Spin Transition and Carrier Type in Rare-Earth Cobaltates via Compositional Complexity. *Adv. Mater.* **2024**, *36*, No. 2406885.
(29) Ishikawa, A.; Nohara, J.; Sugai, S. Raman Study of the Orbital-Phonon Coupling in $LaCoO_3$. *Phys. Rev. Lett.* **2004**, *93*, No. 136401.

https://doi.org/10.1021/acsnano.5c17869
ACS Nano 2026, 20, 6915−6924

(30) Hong, W. T.; Gadre, M.; Lee, Y.-L.; Biegalski, M. D.; Christen, H. M.; Morgan, D.; Shao-Horn, Y. Tuning the Spin State in $LaCoO_3$ Thin Films for Enhanced High-Temperature Oxygen Electrocatalysis. *J. Phys. Chem. Lett.* **2013**, *4*, 2493−2499.
(31) Martín-Carrón, L.; de Andrés, A.; Martínez-Lope, M. J.; Casais, M. T.; Alonso, J. A. Raman phonons as a probe of disorder, fluctuations, and local structure in doped and undoped orthorhombic and rhombohedral manganites. *Phys. Rev. B* **2002**, *66*, No. 174303.
(32) Radaelli, P. G.; Cheong, S.-W. Structural phenomena associated with the spin-state transition in $LaCoO_3$. *Phys. Rev. B* **2002**, *66*, No. 094408.
(33) Abrashev, M. V.; Litvinchuk, A. P.; Iliev, M. N.; Meng, R. L.; Popov, V. N.; Ivanov, V. G.; Chakalov, R. A.; Thomsen, C. Comparative study of optical phonons in the rhombohedrally distorted perovskites $LaAlO_3$ and $LaMnO_3$. *Phys. Rev. B* **1999**, *59*, No. 4146.
(34) Bradicich, A.; Yu, Y.; Brown, T. D.; Jardali, F.; Kumar, S.; Williams, R. S.; Sham-Berger, P. J. Electrically-Driven Metal-Insulator Transitions Emerging from Localizing Current Density and Temperature. *Adv. Electron. Mater.* **2025**, *11*, No. 2400975.
(35) Ridley, B. K. Specific Negative Resistance in Solids. *Proc. Phys. Soc.* **1963**, *82*, No. 954.
(36) Jardali, F.; Chong, J. L.; Yu, Y.; Williams, R. S.; Kumar, S.; Shamberger, P. J.; Brown, T. D. Materials Selection Principles for Designing Electro-Thermal Neurons. *Adv. Electron. Mater.* **2025**, *11*, No. 2400938.
(37) Del Valle, J.; Vargas, N. M.; Rocco, R.; Salev, P.; Kalcheim, Y.; Lapa, P. N.; Adda, C.; Lee, M.-H.; Wang, P. Y.; Fratino, L.; Rozenberg, M. J.; Schuller, I. K. Spatiotemporal characterization of the field-induced insulator-to-metal transition. *Science* **2021**, *373*, 907−911.
(38) Del Valle, J.; Rocco, R.; Domínguez, C.; et al. Dynamics of the electrically induced insulator-to-metal transition in rare-earth nickelates. *Phys. Rev. B* **2021**, *104*, No. 165141, DOI: 10.1103/PhysRevB.104.165141.
(39) Valmianski, I.; Wang, P. Y.; Wang, S.; Ramirez, J. G.; Guénon, S.; Schuller, I. K. Origin of the current-driven breakdown in vanadium oxides: Thermal versus electronic. *Phys. Rev. B* **2018**, *98*, No. 195144.
(40) Madan, H.; Jerry, M.; Pogrebnyakov, A.; Mayer, T.; Datta, S. Quantitative Mapping of Phase Coexistence in Mott-Peierls Insulator during Electronic and Thermally Driven Phase Transition. *ACS Nano* **2015**, *9*, 2009−2017.
(41) Lange, M.; Guénon, S.; Kalcheim, Y.; Luibrand, T.; Vargas, N. M.; Schwebius, D.; Kleiner, R.; Schuller, I. K.; Koelle, D. Imaging of Electrothermal Filament Formation in a Mott Insulator. *Phys. Rev. Appl.* **2021**, *16*, No. 054027.
(42) Bradicich, A.; Brown, T. D.; Ganguli, S.; Williams, R. S.; Shamberger, P. J. Spon-taneous Symmetry-Breaking of Nonequilibrium Steady−States Caused by Nonlinear Electrical Transport. *Adv. Electron. Mater.* **2023**, *9*, No. 2300265.
(43) Kumar, S.; Pickett, M. D.; Strachan, J. P.; Gibson, G.; Nishi, Y.; Williams, R. S. Local Temperature Redistribution and Structural Transition During Joule-Heating-Driven Conductance Switching in VO_2. *Adv. Mater.* **2013**, *25* (42), 6128−6132, DOI: 10.1002/adma.201302046.
(44) Feng, C.; Li, B.-W.; Dong, Y.; Chen, X.-D.; Zheng, Y.; Wang, Z.-H.; Lin, H.-B.; Jiang, W.; Zhang, S.-C.; Zou, C.-W.; Guo, G.-C.; Sun, F.-W. Quantum imaging of the re-configurable VO_2 synaptic electronics for neuromorphic computing. *Sci. Adv.* **2023**, *9*, No. eadg9376.
(45) Bortnikov, S. G.; Aliev, V. S.; Badmaeva, I. A.; Mzhelskiy, I. V. VO_2 film temperature dynamics at low-frequency current self-oscillations. *J. Appl. Phys.* **2018**, *123*, No. 075701.
(46) Bidoul, N.; Roisin, N.; Flandre, D. Tuning the Intrinsic Stochasticity of Resistive Switching in VO_2 Microresistors. *Nano Lett.* **2024**, *24*, 6201−6209.
(47) Sun, J. R.; Li, R. W.; Shen, B. G. Spin-state transition in La1xSmxCoO3 perovskites. *J. Appl. Phys.* **2001**, *89*, 1331−1335.
(48) Zhang, A. C.; Álvarez-Chico, A.; Salagre, E.; Gonzalez, M.; Spataru, C. D.; Sugar, J. D.; Gross, A. L.; González-Barrio, M. A.; Segovia, P.; Tallarida, M.; Dai, J.; Kumar, S.; Talin, A. A.; Hwang, H. Y.; Michel, E. G.; Mascaraque, A.; Fuller, E. J. Dynamic Doping of Nickelates with Lithium Reveals a Widely Tunable Insulator−Metal Tran-sition with Charge Filling and Band Renormalization Regimes. *ACS Nano* **2025**, *19*, 28422−28431.
(49) Del Valle, J.; Salev, P.; Tesler, F.; Vargas, N. M.; Kalcheim, Y.; Wang, P.; Trastoy, J.; Lee, M.-H.; Kassabian, G.; Ramírez, J. G.; Rozenberg, M. J.; Schuller, I. K. Subthresh-old firing in Mott nanodevices. *Nature* **2019**, *569*, 388−392.
(50) Janzakova, K.; Balafrej, I.; Kumar, A.; Garg, N.; Scholaert, C.; Rouat, J.; Drouin, D.; Coffinier, Y.; Pecqueur, S.; Alibart, F. Structural plasticity for neuromorphic net-works with electropolymerized dendritic PEDOT connections. *Nat. Commun.* **2023**, *14*, No. 8143.
(51) Maryada; Soldado-Magraner, S.; Sorbaro, M.; Laje, R.; Buonomano, D. V.; Indiveri, G. Stable recurrent dynamics in heterogeneous neuromorphic computing systems using excitatory and inhibitory plasticity. *Nat. Commun.* **2025**, *16*, No. 5522.
(52) Tahouni-Bonab, F.; Hepting, M.; Luibrand, T.; Cristiani, G.; Schmid, C.; Logvenov, G.; Keimer, B.; Kleiner, R.; Koelle, D.; Guénon, S. Nonvolatile multistate electrother-mal resistive switching in a strongly correlated insulator thin-film device. *Phys. Rev. Appl.* **2025**, *24*, No. 034014.

https://doi.org/10.1021/acsnano.5c17869
ACS Nano 2026, 20, 6915−6924

Electrothermally-Induced Channel Formation in a Spin-Crossover Neuron

Elena Salagre[†1], Mahnaz Islam[†1, 2], Yeonju Yu[3], Sanjana Goyal[1,4], Timothy D. Brown[1], Fatme Jardali[3], Sangheon Oh[1], Eric Pop[2], R. Stanley Williams[5], A. Alec Talin[1], Suhas Kumar[1], Patrick J. Shamberger[3], and Elliot J. Fuller*[1]

[1]Sandia National Laboratories, 7011 East Ave, Livermore, CA, 94550 USA
[2]Department of Electrical Engineering, Stanford University, Stanford, CA, 94305, USA
[3]Department of Materials Science and Engineering, Texas A&M University, College Station 77843-3003, TX, USA
[4]Department of Engineering Science, UC Berkeley, Berkeley, CA 94720, USA
[5]Department of Electrical and Computer Engineering, Texas A&M University, College Station 77843-3128, TX, USA

† *Authors contributed equally*
* *Corresponding author*

1 Supplementary IV curves

I-V curves corresponding to a subset of the studied device geometries is shown in Figure S1. We note all geometries studied behaved similarly and were reproducible.

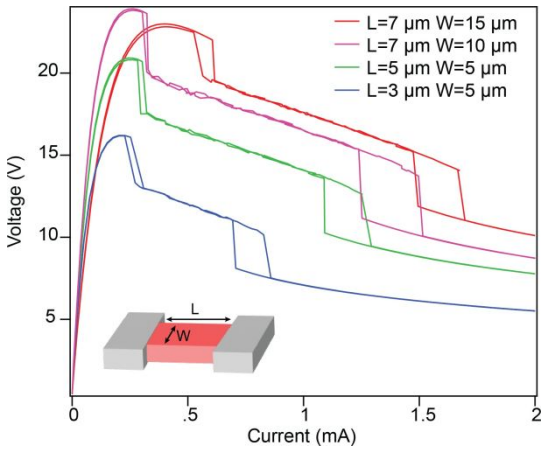

Figure S 1: IVs for different size devices showing the dependency on width and length.

2 Temperature Raman Calibration

In order to understand the observed changes in operando devices, thin films of LCO of equivalent growth to the devices shown have been studied at different temperatures. The Raman analysis is shown in Figure S2.

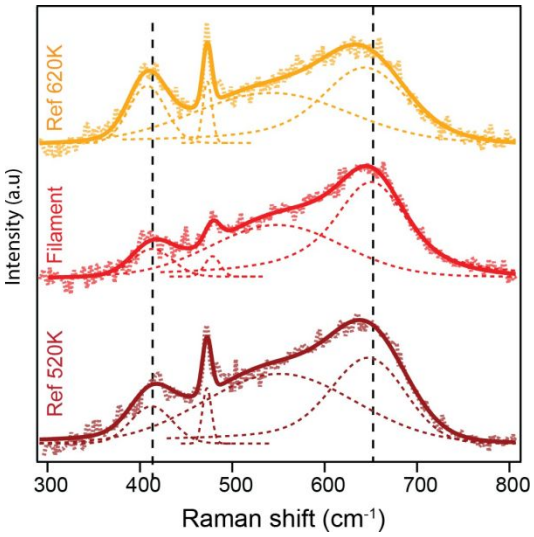

Figure S 2: Raman spectra and peak fitting of temperature dependent LCO thin film at 520 K and 620 K and comparison with signal extracted from active conduction channel (central spectra). Fitting has been done using A_{2g}, E_g, 400 cm^{-1} and LAO peaks.

3 Conduction Channel Shape and Size

The conduction channel, sometimes referred to as conductive filament or current path, has been investigated for a range of device sizes and applied currents. This region is defined as the portion of material in the otherwise insulating device that is acting as the conduction channel for most of the current flow through the device. This also implies that this region has higher conductivity (metallic character) and higher temperature. This conduction channels usually forms a longitudinal path across the electrodes. The conduction channels studied here are volatile and rely on the localized MIT present in the material. In order to corroborate channel shape and size, some devices were switching above the non-volatile damage threshold, generating a region with optical contrast were the hot channel formed. This region is visible with optical microscopes (as shown in Figure S3c) and is not subject to the *operando* resolution limitations, therefore presenting the most reliable channel size and shape. We note that damage thresholds depend on applied bias, external circuit and bias hold duration.

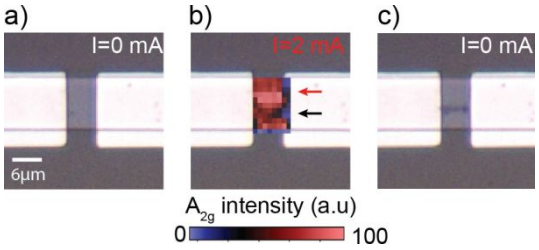

Figure S 3: Optical images before a) and after c) a permanent damage is created due to conduction channel formation at high current bias. Panel b) optical image has a 2D Raman map of the A_{2g} mode intensity during regime III, comparable to Figure 2c of main text.

A bibliographic survey has been performed for reported conduction channels or filaments formation in MIT based devices. Figure S4 shows our method of width determination and a comparison to previous data in VO_x channels. We note that, in the bibliography we are including voltage and current controlled devices and that power dissipation has been estimated from the provided data in each case to the best of our knowledge. LCO is shown in gray and black with error bars, while VO_2 (red) V_2O_3 (green) and V_3O_5 (blue) markers correspond to different bibliography sources as: squares [1], filled circles [2], stars [3], empty circles [4], empty squares [5], inverted triangles [6] and diamonds [7]. We note that power dissipation is the main source of channel or filament width trends in the literature, however, domain coexistence for the case of first order transition materials should be considered independently.

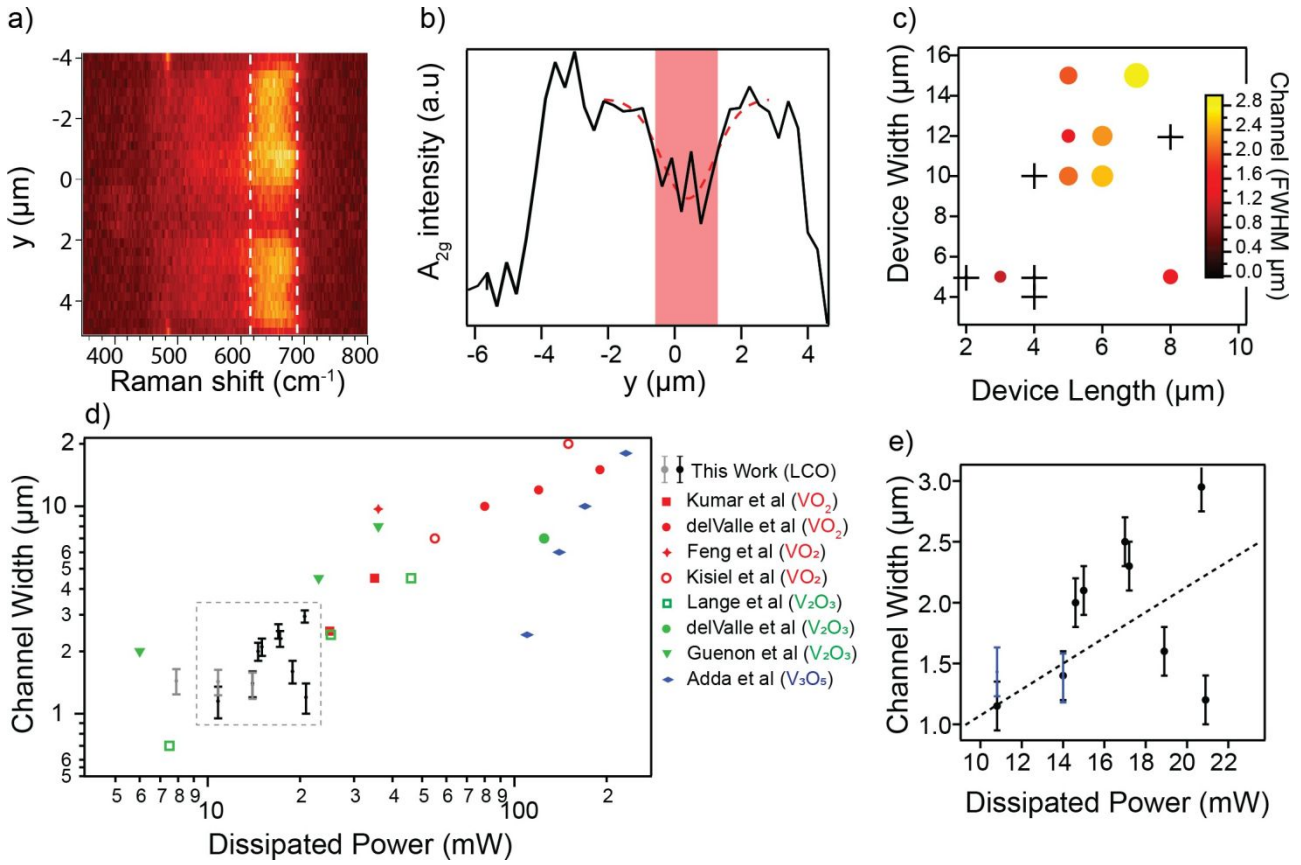

Figure S 4: Conduction channel size analysis from Raman images at 2 mA bias (Regime III) for different size devices. Panels a) and b) correspond to analysis process using A_{2g} profile across the channel and gaussian fitting with FWHM value extraction. Panel c) shows the conduction channel width (color and size of dots). Note that crosses in c) indicate device studied but channel width fitting inconclusive. Panel d) shows conduction channel width as a function of dissipated power including data extracted from numerous bibliography sources for vanadium oxides. We note the lower powers needed for our LCO devices are consistent with the trend of larger channels with increasing dissipated power. Dissipated powers and channel widths from references have been estimated from reported data, including voltage and current values, and therefore have unknown error bars. Panel e) shows a zoom on our reported data from this work, including data obtained from different devices (black) and different I_{app} (blue).

4 Supplementary Raman images

In this section additional Raman images of *operando* devices are shown. This serves as a reproducibility and variability analysis, as well as including data for slightly different geometry and current conditions.
Additional examples of devices in regime II and III are shown in Figure S5. The different types of regime II discussed in the main text can be identified in the top row, while consistency in regime III is shown in the bottom row. Note that different size devices are used, the scale bars at the left of each image shows 5 μm vertical dimension to aid comparison.

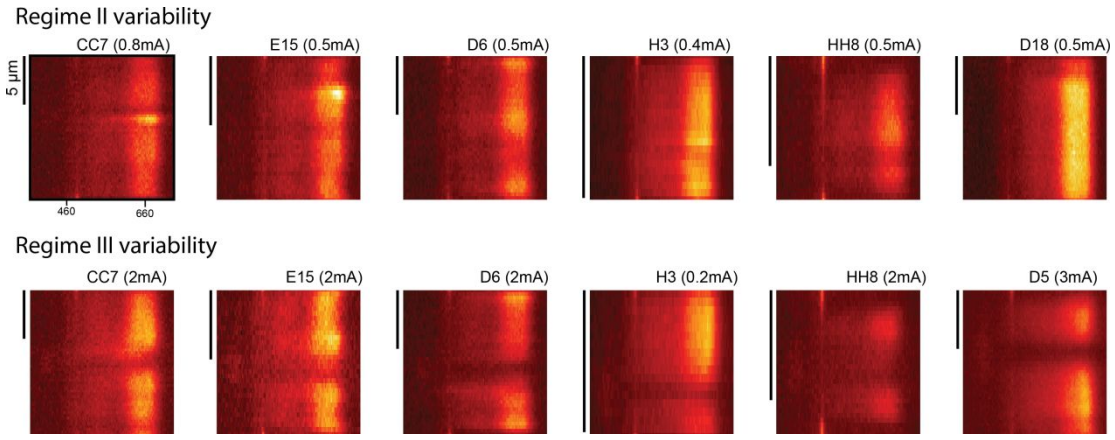

Figure S 5: Variability of regime II (top row) and regime III (bottom row) device identification and voltage underneath each image. Scale bar of 5 µm shown at the left side of each image to aid comparison between different width devices.

Figure S6 shows additional points in the I-V curve of a representative device, with images in regimes I, II and III.

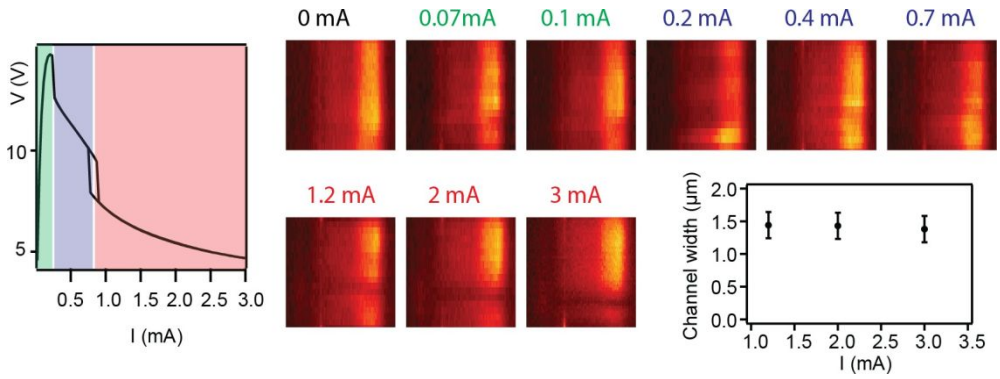

Figure S 6: Evolution of Raman maps with bias. Increasing current from left to right. 0.0 A leftmost image for reference of unbiased case. 0.07 and 0.1 mA correspond to regime I. 0.2, 0.4 and 0.7 mA correspond to regime II during oscillations. 1.2, 2 and 3 mA correspond to regime III. The corresponding IV curve of the device (L=3 μm W=5μm) is shown in the left for reference. In the bottom right, the relationship between conduction channel width and applied bias for the three cases in regime III is shown to be almost constant.

5 Regime II: Self-Oscillations

A study of oscillation shape, duration and frequency is shown for a representative device in Figure S7. The frequency and width of on-state vs bias dependency is shown as an inset. This behavior is reproduced for all devices studied. The complex interaction between the thermal and electrical conductivities as a function of temperature are made evident by the complexity of the observed oscillatory behavior and are topics of future discussion.

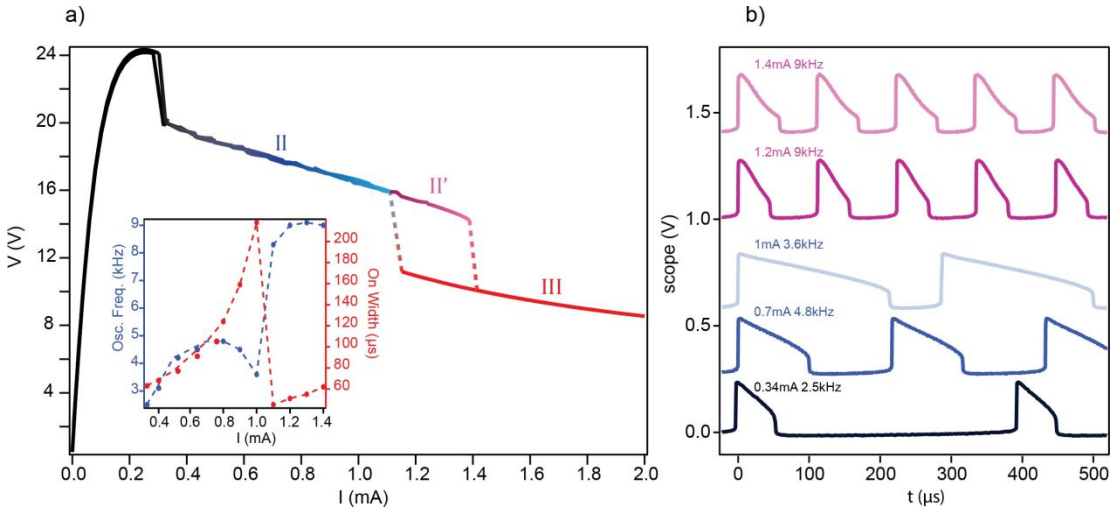

Figure S 7: IV curve and oscillation dynamics of a representative device. The full I-V curve of the device is shown. Oscillations for representative points of regime II are shown in the right panel.

6 Supplementary IR camera images

IR images of a uniform device during oscillation are shown in Figure S8. Limited spatial resolution makes the identification of the hopping channel difficult. Despite the lower spatial resolution, the temperature distribution observed in the IR camera is in agreement with the observed changes in Raman images.

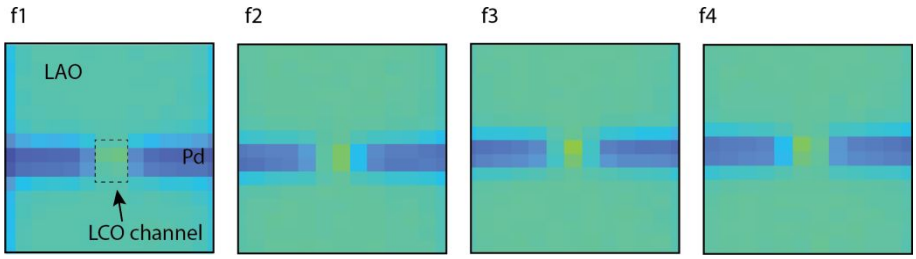

Figure S 8: Thermal camera of a uniform device with etched LCO channel during oscillations. Each image corresponds to a peak of an oscillation. Color scale has been chosen to aid identification of different position in the conduction channel formation.

Figure S9 shows the total IR counts during a full cycle of oscillation, highlighting the time resolution in addition to spatial resolution.

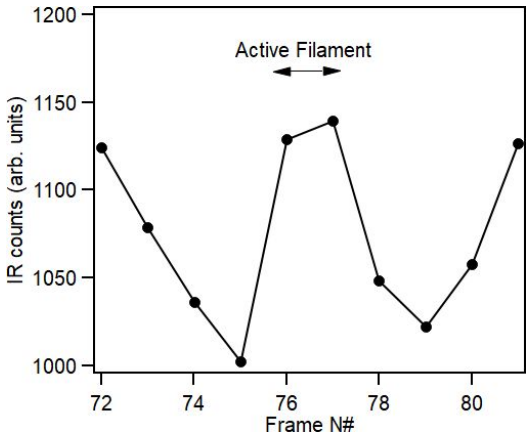

Figure S 9: Integrated total thermal counts in channel by frame of the FLIR thermal camera. Data obtained in a L= 6 µm W=12 µm device under a current bias corresponding to the oscillating NDR (Regime II).

7 Bistable devices

Detail of the bistable IR experiments are shown in Figures S10 and S11. The I-V ramp and chosen frames discussed in the main text can be seen, as well as the analysis of the path position and probability distribution.

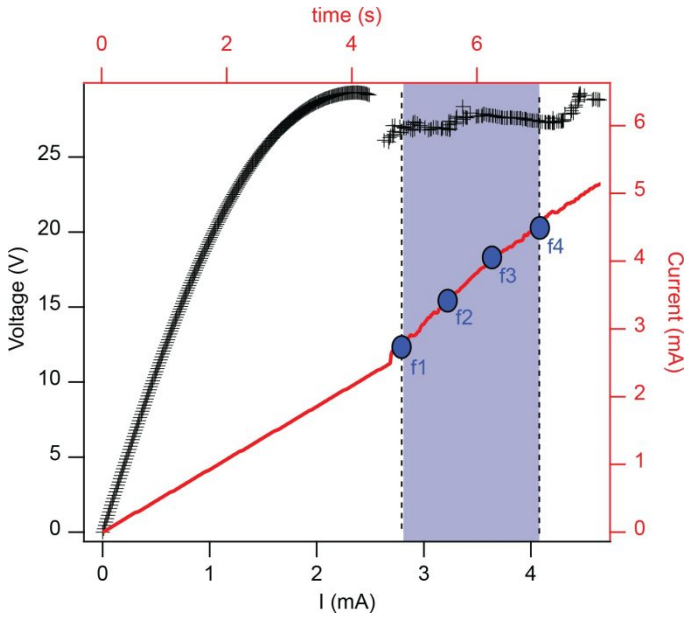

Figure S 10: Voltage vs applied current (black) and applied current vs time (red) for the oscillating device shown in main text Figure 4c. The shaded blue region corresponds to the region studied in panels d) and e) of that same figure, while blue dots correspond to the chosen frames. Frame rate was set to 60 Hz with a spatial resolution of 10 μm. Note the device geometry and external circuit shifts the current thresholds for this specific device.

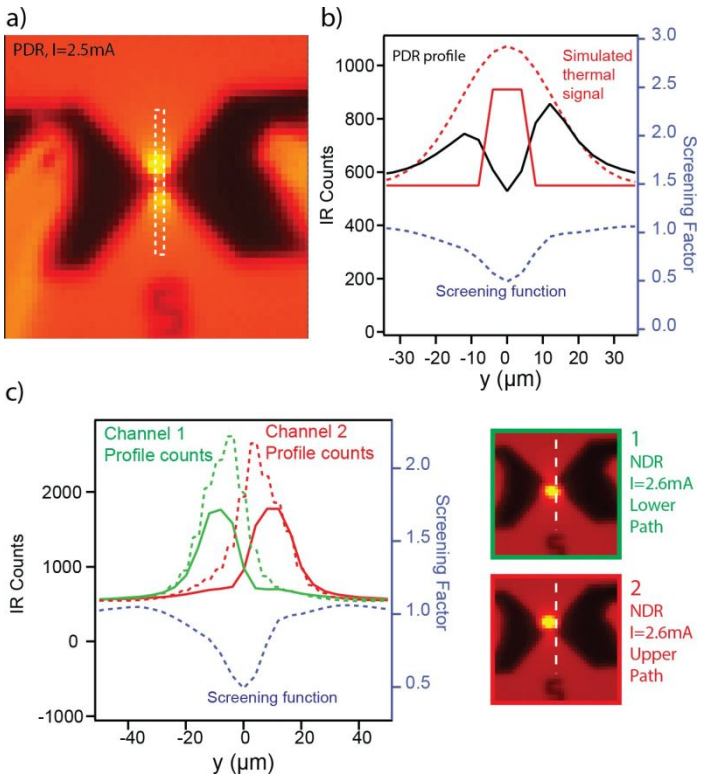

Figure S 11: Bistable IR counts analysis. Panel a) IR thermal image of bistable device in PDR before current collapse. Panel b) corresponds to profile extracted from white dashed rectangular region in a), simulated thermal counts from channel (red), gaussian broadening of that signal (dashed red) and extracted screening function. Panel c) shows profiles extracted for frames with conduction channels in the upper (red) and lower (green) paths shown in the images in the bottom right. Raw data has been corrected by the screening function in b) to generated simulated IR counts from the conductive paths (dashed green and red curves).

Using a profile extracted from Figure S11a, when the device is at PDR, we have extracted the screening of counts due to the metal electrodes by considering a simulated real signal of a step function convoluted with a 15 μm Gaussian, due to resolution limitations. This function is used to correct raw counts from IR images showing upper and lower conduction paths. With this analysis, the distance between conduction channels is approximately 8 μm, closer to the expected value of 5 μm from simulations.

8 Volatility and memory effects

Additional results for non-volatile effects are shown. Figure S12a, b and c show a device volatility when switched in regime II and short-term non-volatility when switched in regime III for a long period. Figure S12d and e show the effect of this non-volatility in the bistable devices, inducing a preference for one of the two paths (panel e).

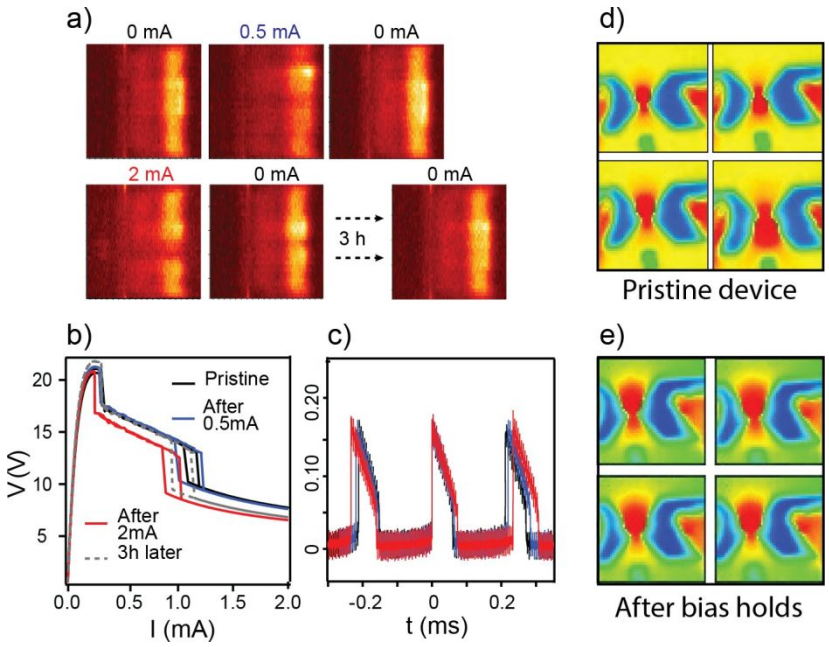

Figure S 12: a) Volatility (top row) and semi-volatility (bottom row) comparison. Pristine 0 mA Raman map in top left image. Top row shows volatility of regime II while bottom row shows short term plasticity after biasing at 2 mA, last image shows the loss of this effect. b) and c) show the changes in IV and oscillations of a semi-permanent signature. d) and e) correspond to thermal camera images of a bistable device during oscillations for the pristine device showing bistability in d) and a device with a semi-permanent signature in which the conduction channel always forms in the top path.

9 Supplementary model and calculations

9.1 Model Parameters

	$LaAlO_3$ (substrate)	**Pd**	**$LaCoO_3$**
$\sigma(T)$ (S/m)	N/A	$95 \cdot 10^5$*	Exp
κ(T) (W/mK)	10	71.2*	*
C_p (T) (J/kgK)	467*	247*	*
ρ (g/cm^3)	6.52	12.01*	7.35
Relative Permittivity	N/A	0*	15

Table S 1: The interlayer conductance between LCO and LAO is $800 \cdot 10^6$ (W/m^2K), and LCO Molar mass is 245.836 (g/mol). * Literature sources include: [8–10]

9.1.1 Governing Equations

The law of heat conduction (Fourier's law),

$$q = -K\nabla T \tag{1}$$

where q (W/m^2) is the heat flux density and ρ denotes thermal conductivity W/mK). Coupling this into the electric current system, which adds the heat source term $Q_e(W/m^3)$ to account for resistive heating in the heat equation:

$$\rho C_p \frac{\delta T}{\delta t} - \nabla(K\nabla T) = Q_e \tag{2}$$

The different quantities involved here are recalled below:
ρ: Density (kg/m^3)
C_p: Specific heat capacity at constant stress (J/(kg K)
κ: Thermal Conductivity (W/m K)
The resistive heating (ohmic heating) due to the electric current (W/m^3) is

$$Q_e = J \cdot E \tag{3}$$

Where J represents the electric current density (A/m^2) and E is the electric field (N/C or V/m).

9.1.2 Sensitivity Analysis

For the sensitivity analysis, parameters have been individually changed to obtain their effect on the conduction channel width. Table S2 summarizes the change from LCO reference values (FWHM=3.93 μm and maximum temperature T_{max}=410.57 K) when individually changing the model parameters.

	ΔK_F (K)	σ_F LT (S/m)	σ_F HT (S/m)	$\Delta\sigma_F$ (S/cm)	κ_F (W/mK)	κ_S (W/mK)	d_F (nm)	d_S (nm)
Parameter Change	500 → 250	[1 →2] $\cdot 10^2$	[1 →2] $\cdot 10^5$	[1 →2] $\cdot 10^5$	[1.1 - 2.6] → [2.2 - 5.2]	10 → 20	140 → 280	20 → 40
FWHM	0.71	4.73	2.17	4.38	5.42	1.09	1.98	5.08
T_{max}	603.85	399.81	424.23	385.32	391.22	479.68	426.17	401.53

Table S 2: Where ΔK is the width of the sigmoid (transition) σ is conductivity, κ is thermal conductivity and d is thickness. The subindex F and S correspond to film and substrate respectively. All simulations are run with the same applied current of 2.0 mA in a W=12 L=7 μm device to reproduce our experimental results.

The results of the sensitivity analysis suggest that the substrate contribution to the conduction channel width is not the source of the observed trend between reported VO_2 conduction channels and the results presented in this work. The LAO substrate relatively low thermal conductivity. Furthermore, the substrate conductivity increase has the opposite effect. Additionally, we have run simulations using LCO and VO_2 as film material and two different device configurations and geometries, as shown in Table S3. This effort has been made to rule out external parameters not directly link to the active material, including changes in device size and film thickness. The geometries compared (G1 and G2) use $LaAlO_3$ and sapphire (Al_2O_3) as substrates, as these are commonly used in each material growth. Substrate thickness is fixed to 20 μm for all cases. The first column of results corresponds to our experimental system. Simulations with slightly higher I_{app} for the larger geometry (G2) are also shown for completeness.

Material	LCO		VO_2	
ΔK_F (K)	500		20	
σ_F LT (S/m)	$1\cdot 10^2$		$2\cdot 10^3$	
σ_F HT (S/m)	$1\cdot 10^5$		$1\cdot 10^6$	
T_{IMT} (K)	500		340	
κ_F (W/mK)	1.1 - 2.6		3.6 - 5.5	
κ_S (W/mK)	10		30	
Geometry	G1	G 2	G1	G 2
L (μm)	7	20	7	20
W (μm)	12	20	12	20
d_F (nm)	140	100	140	100

Results	LCO G1	LCO G2		VO_2 G1	VO_2 G2	
I_{app} (mA)	2	2	2.5	2	2	2.5
FWHM (μm)	3.93	9.90	9.85	9.37	15.80	11.76
T_{max} (K)	410.57	388.95	401.19	320.32	320.04	326.6

Table S 3: Role of geometry and material in simulations. I_{app} is current applied, L is device length, W is device width. T_{IMT} is the temperature of the IMT transition.

9.2 Strain components

The thermal ($\epsilon_{th}=\alpha(T-T_{ref})$, where α is the coefficient of thermal expansion) and elastic (ϵ_e) strain components for the LCO film have been calculated using the LCO thermal expansion and elasticity matrix.

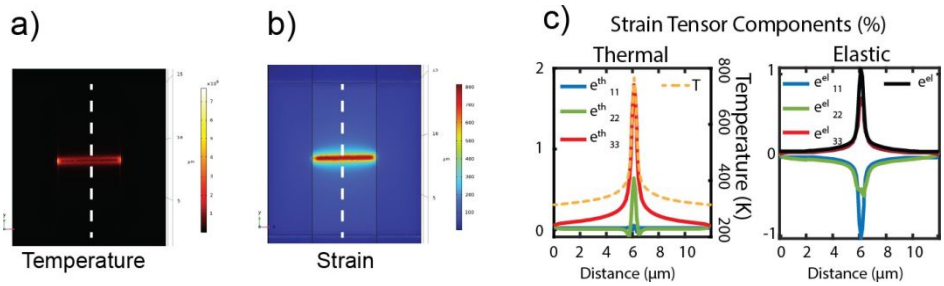

Figure S 13: Panels a) and b) are steady state temperature and strain distributions in a L=5 W=15 LCO device like the one shown in Figure 4 main text. Panel c) shows thermal and elastic strain tensor components along the white dotted line cuts in a) and b).

Panels a, b and c show simulated temperature and strain distributions during active static conduction channel in a LCO device. Extracting profiles perpendicular to the current flow in the center of the channel, similarly to the experimental measurements, we can observe how the very sharp concentration of high temperature (dotted orange line in the left graph of panel c) is accompanied by localized strain, both thermal and elastic strain components show distributions centered in the metallic hot region. Interestingly, in plane components of thermal strain show a small degree of compressive strain in the boundaries of the conduction channel, while being highly tensile in the center both in plane and out of plane. Elastic strain is also considered, being tensile out of plane and compressive in plane. In part, large strain gradients may explain the non-temperature effects observed in Raman spectra, where A_{2g} shifts and increases in signal appear at the edges of the conduction channel.

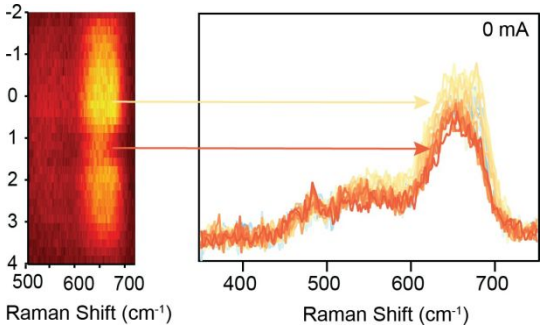

Figure S 14: Extracted Raman profiles at different positions for a semi-volatile signature.

References

[1]S. Kumar, M. D. Pickett, J. P. Strachan, G. Gibson, Y. Nishi, and R. S. Williams, "Local temperature redistribution and structural transition during joule-heating-driven conductance switching in VO_2", 10.1002/adma.201302046(2013) 10. 1002/adma.201302046.

[2]J. del Valle, N. M. Vargas, R. Rocco, et al., "Spatiotemporal characterization of the field-induced insulator-to-metal transition", Science **373**, 907–911 (2021) 10.1126/science.abd9088.

[3]C. Feng, B.-W. Li, Y. Dong, et al., "Quantum imaging of the reconfigurable VO_2 synaptic electronics for neuromorphic computing", Science Advances **9**, eadg9376 (2023) 10.1126/sciadv.adg9376.

[4]E. Kisiel, P. Salev, I. Poudyal, et al., "High-resolution full-field structural microscopy of the voltage-induced filament formation in VO_2-based neuromorphic devices", ACS nano **19**, 15385–15394 (2025) 10.1021/acsnano.4c14696.

[5]M. Lange, S. Guénon, Y. Kalcheim, et al., "Imaging of Electrothermal Filament Formation in a Mott Insulator", Physical Review Applied **16**, 054027, 054027 (2021) 10.1103/PhysRevApplied.16.054027.

[6]S. Guénon, S. Scharinger, S. Wang, et al., "Electrical breakdown in a V_2O_3 device at the insulator-to-metal transition", Europhysics Letters **101**, 57003 (2013) 10.1209/0295-5075/101/57003.

[7]C. Adda, M.-H. Lee, Y. Kalcheim, et al., "Direct observation of the electrically triggered insulator-metal transition in v_3o_5 far below the transition temperature", Physical Review X **12**, 011025 (2022) 10.1103/PhysRevX.12.011025.

[8]Y. Zhang, W. M. Postiglione, R. Xie, et al., “Wide-range continuous tuning of the thermal conductivity of la0.5sr0.5coo3- films via room-temperature ion-gel gating”, Nature Communications **14**, 2626 (2023) 10.1038/s41467-023-38312-z.

[9]G.-J. Shu, P.-C. Wu, and F. C. Chou, “The spin–orbit–phonon coupling and crystalline elasticity of LaCoO3 perovskite”, RSC Advances **10**, 43117–43128 (2020) 10.1039/D0RA09675J.

[10]P. C. Michael, J. U. Trefny, and B. Yarar, “Thermal transport properties of single crystal lanthanum aluminate”, Journal of Applied Physics **72**, 107–109 (1992) 10.1063/1.352166.